Monthly Notices
of the
ROYAL ASTRONOMICAL SOCIETY

MNRAS **513,** 4159–4168 (2022)
Advance Access publication 2022 April 28

https://doi.org/10.1093/mnras/stac1167

Prospects for multimessenger detection of binary neutron star mergers in the fourth LIGO–Virgo–KAGRA observing run

Barbara Patricelli,[1,2,3,4★] Maria Grazia Bernardini,[5★] Michela Mapelli,[6,7,8] Paolo D'Avanzo,[5] Filippo Santoliquido,[6,7] Giancarlo Cella,[3] Massimiliano Razzano[1,3] and Elena Cuoco[2,3,9]

[1]*Physics Department, University of Pisa, Largo B. Pontecorvo 3, I-56127 Pisa, Italy*
[2]*European Gravitational Observatory, Via E. Amaldi, I-56021 Cascina, Pisa, Italy*
[3]*INFN – Pisa, Largo B. Pontecorvo 3, I-56127 Pisa, Italy*
[4]*INAF – Osservatorio Astronomico di Roma, Via Frascati 33, I-00078 Monte Porzio Catone, Rome, Italy*
[5]*INAF – Osservatorio Astronomico di Brera, Via Bianchi 46, I-23807 Merate, Lecco, Italy*
[6]*Physics and Astronomy Department Galileo Galilei, University of Padova, Vicolo dell'Osservatorio 3, I-35122 Padova, Italy*
[7]*INFN – Padova, Via Marzolo 8, I-35131 Padova, Italy*
[8]*INAF – Osservatorio Astronomico di Padova, Vicolo dell'Osservatorio 5, I-35122 Padova, Italy*
[9]*Scuola Normale Superiore (SNS), Piazza dei Cavalieri 7, I-56126 Pisa, Italy*

Accepted 2022 April 23. Received 2022 April 22; in original form 2021 December 17

ABSTRACT

The joint detection of GW170817 and GRB 170817A opened the era of multimessenger astronomy with gravitational waves (GWs) and provided the first direct probe that at least some binary neutron star (BNS) mergers are progenitors of short gamma-ray bursts (S-GRBs). In the next years, we expect to have more multimessenger detections of BNS mergers, thanks to the increasing sensitivity of GW detectors. Here, we present a comprehensive study on the prospects for joint GW and electromagnetic observations of merging BNSs in the fourth Laser Interferometer Gravitational-wave Observatory (LIGO)–Virgo–Kamioka Gravitational Wave Detector (KAGRA) observing run with *Fermi Gamma-ray Space Telescope* (*Fermi*), *Neil Gehrels Swift Observatory* (*Swift*), *INTErnational Gamma-Ray Astrophysics Laboratory* (*INTEGRAL*), and *Space Variable Objects Monitor* (*SVOM*). This work combines accurate population synthesis models with simulations of the expected GW signals and the associated S-GRBs, considering different assumptions about the gamma-ray burst (GRB) jet structure. We show that the expected rate of joint GW and electromagnetic detections could be up to $\sim$6 yr^{-1} when *Fermi*/Gamma-ray Burst Monitor (GBM) is considered. Future joint observations will help us to better constrain the association between BNS mergers and S-GRBs, as well as the geometry of the GRB jets.

Key words: gravitational waves – gamma-ray bursts – neutron star mergers.

1 INTRODUCTION

On 2017 August 17, Advanced Laser Interferometer Gravitational-wave Observatory (LIGO; Aasi et al. 2015) and Advanced Virgo (Acernese et al. 2015) observed for the first time a gravitational wave (GW) signal from the inspiral of a binary neutron star (BNS) merger (GW170817; Abbott et al. 2017a); less than 2 s after, a short gamma-ray burst (S-GRB), GRB 170817A, was observed by *Fermi Gamma-ray Space Telescope* (*Fermi*)/Gamma-ray Burst Monitor (GBM; Goldstein et al. 2017) and *INTErnational Gamma-Ray Astrophysics Laboratory* (*INTEGRAL*; Savchenko et al. 2017). Besides the discovery of gamma-ray burst (GRB) afterglow in the X-rays and radio band (Hallinan et al. 2017; Troja et al. 2017), the electromagnetic follow-up of GW 170817 also led to the discovery and characterization of the bright kilonova AT2017gfo (Coulter et al. 2017; Pian et al. 2017; Smartt et al. 2017; Tanvir et al. 2017). This joint detection marked the beginning of multimessenger astronomy with GWs and provided the first direct evidence that BNS mergers are progenitors of S-GRBs (Abbott et al. 2017b). The joint observation of GW170817 and GRB 170817A also allowed astrophysicists to infer some basic properties of S-GRB jets. For instance, long baseline interferometry observations put constraints on the source size and its displacement that were found to be consistent with expectations for a structured relativistic jet (Mooley et al. 2018; Ghirlanda et al. 2019). During the first half of their third observing run (O3a), Advanced LIGO and Advanced Virgo observed another potential BNS merging system: GW190425 (Abbott et al. 2020b), but no electromagnetic (EM) signal was found in association with this event (see e.g. Hosseinzadeh et al. 2019). However, it would have been difficult to detect an EM counterpart to GW190425, given its poor sky localization and larger distance compared with GW170817.

Here, we present the prospects for joint GW and EM detection of BNS merging systems in the next observing run (O4) of the GW detector network (Abbott et al. 2020a) composed of Advanced LIGO, Advanced Virgo, and Kamioka Gravitational Wave Detector (KAGRA; Akutsu et al. 2019), with a particular focus on the prospects for the joint detection of a GW signal and of the emission of an S-GRB. In fact, during O4 the GW interferometers will operate with increased sensitivity, and the synergy with the facilities that are

★ E-mail: barbara.patricelli@pi.infn.it (BP); maria.bernardini@inaf.it (MGB)

capable to trigger, locate, and rapidly deliver the main characteristics of the S-GRB in nearly real time will be crucial for the unambiguous identification of the EM counterpart of the GW events, and for the follow-up at different wavelengths. These facilities such as the *Fermi* (Ritz 2007), *INTEGRAL* (Winkler et al. 2003), and the *Neil Gehrels Swift Observatory* (*Swift*; Gehrels et al. 2004) will also be complemented by new EM detectors such as the Sino–French space mission *Space Variable Objects Monitor* (*SVOM*; Wei et al. 2016) that will start taking data during the O4 observing run (mid-2023). This unique combination of GW and EM facilities will be the key to further probe the physics and astrophysics of BNS systems.

Our investigation combines accurate population synthesis models with simulations of the expected GW signals. The associated S-GRB emission is calculated with general assumptions on the S-GRB population and testing different possible models for the jet structure to include also slightly off-axis events. This paper is organized as follows. In Section 2, we describe the theoretical models used to simulate the population of BNS merging systems. Sections 3 and 4 present our simulation and analysis pipelines for GW signals and S-GRBs. In Section 5, we present our results. Finally, Section 6 discusses our results and summarizes our conclusions.

2 THE BNS POPULATION

We generate a sample of synthetic BNSs populating the local Universe up to a redshift $z = 0.11$ that is consistent with the expected horizon[1] for BNS mergers of Advanced Virgo and Advanced LIGO in the O4 configuration (Abbott et al. 2020a).

We obtained our catalogues of synthetic BNSs with the MOBSE population-synthesis code (the acronym MOBSE stands for massive objects in binary stellar evolution; see e.g. Mapelli et al. 2017; Giacobbo & Mapelli 2018; Giacobbo, Mapelli & Spera 2018). MOBSE is an upgraded version of the code BSE (binary stellar evolution; see Hurley, Tout & Pols 2002), including an up-to-date formalism for the winds of massive hot stars (O-type, B-type, Wolf–Rayet, and luminous blue variable stars), which describes the mass-loss rate as $\dot{M} \propto Z^{\beta}$ for all massive hot stars, where

$$\beta = \begin{cases} 0.85 & \text{if} \quad \Gamma_{\rm e} < 2/3, \\ 2.45 - \Gamma_{\rm e}\, 2.4 & \text{if} \quad 2/3 \leq \Gamma_{\rm e} \leq 1, \\ 0.05 & \text{if} \quad \Gamma_{\rm e} > 1. \end{cases} \tag{1}$$

In equation (1), $\Gamma_{\rm e}$ is the Eddington ratio for electron scattering (see Giacobbo et al. 2018 for details).

For the outcome of core-collapse supernovae we use the delayed model discussed by Fryer et al. (2012), which does not produce any mass gap between neutron stars (NSs) and black holes. Furthermore, MOBSE treats electron-capture and (pulsational) pair-instability supernovae as described in Giacobbo & Mapelli (2019) and Mapelli et al. (2020), respectively. We model natal kicks as

$$v_{\rm kick} = f_{\rm H05}\, \frac{m_{\rm ej}}{\langle m_{\rm ej} \rangle}\, \frac{\langle m_{\rm NS} \rangle}{m_{\rm rem}}, \tag{2}$$

where $f_{\rm H05}$ is a random number extracted from a Maxwellian distribution with one-dimensional root-mean-square $\sigma_{\rm kick} = 265$ km s^{-1} (Hobbs et al. 2005), $m_{\rm rem}$ is the mass of the compact remnant (NS or black hole), $m_{\rm ej}$ is the mass of the ejecta, while $\langle m_{\rm NS} \rangle$ is the average NS mass, and $\langle m_{\rm ej} \rangle$ is the average mass of the ejecta associated with the formation of a NS of mass $\langle m_{\rm NS} \rangle$ from single stellar evolution. In our calculations, we adopt $\langle m_{\rm NS} \rangle = 1.3$ M$_\odot$ and $\langle m_{\rm ej} \rangle = 9$ M$_\odot$, respectively. As discussed in Giacobbo & Mapelli (2020), equation (2) can be used for both NSs and black holes, produces lower kicks for ultrastripped supernovae (Tauris et al. 2013, 2017; Tauris, Langer & Podsiadlowski 2015), matches the distribution of proper motions of young pulsars in the Milky Way (Hobbs et al. 2005) and the merger rate density inferred by the LIGO–Virgo Collaboration (Abbott et al. 2021). Binary evolution has been implemented in MOBSE adopting the formalism by Hurley et al. (2002).

For this work, we ran three sets of simulations with MOBSE, corresponding to three different choices of the common envelope parameter $\alpha = 1$, 3, and 7 (Hurley et al. 2002). The α parameter encodes the efficiency of common envelope ejection: a large value of α means that the envelope can be efficiently removed from the binary system (Webbink 1984). Here, we choose these three values of α, because they approximately bracket current uncertainties on the merger rate (see the discussion below). In all our models, we assume that main-sequence and Hertzsprung gap stars cannot survive a common envelope phase. For the other stellar types, we calculate common envelope as described in Hurley et al. (2002). Each simulation set is composed of 12 metallicities $Z = 0.0002$, 0.0004, 0.0008, 0.0012, 0.0016, 0.002, 0.004, 0.006, 0.008, 0.012, 0.016, and 0.02. We simulated 10^7 binary stars per each metallicity. Primary masses follow a Kroupa initial mass function (Kroupa 2001) between 5 and 150 M$_\odot$. The values of orbital period, eccentricity, and mass ratio are drawn from Sana et al. (2012). In particular, we derive the mass ratio $q = m_2/m_1$ as $\mathcal{F}(q) \propto q^{-0.1}$ with $q \in [0.1,\ 1]$, the orbital period P from $\mathcal{F}(\Pi) \propto \Pi^{-0.55}$ with $\Pi = \log_{10}(P/{\rm d}) \in [0.15,\ 5.5]$ and the eccentricity e from $\mathcal{F}(e) \propto {\rm e}^{-0.42}$ with $0 \leq e \leq 0.9$.

From these runs, we derived catalogues of BNS masses and delay times, i.e. the time elapsed from the formation of a binary star to its merger. In order to derive the redshift of each merger, we fed these quantities to our code COSMO$\mathcal{R}$ATE (Santoliquido et al. 2020). COSMO$\mathcal{R}$ATE calculates the BNS merger rate density evolution in the comoving frame and then associates a redshift of formation and merger to the simulated BNSs, as described in Santoliquido et al. (2021). In particular, COSMO$\mathcal{R}$ATE estimates the cosmic merger rate density $\mathcal{R}(z)$ in the comoving frame as

$$\mathcal{R}(z) = \frac{{\rm d}}{{\rm d}t(z)} \times \left[\int_{z_{\rm max}}^{z} \psi(z')\, \frac{{\rm d}t(z')}{{\rm d}z'}\, {\rm d}z' \int_{Z_{\rm min}}^{Z_{\rm max}} \eta(Z)\, \mathcal{F}(z', z, Z)\, {\rm d}Z \right], \tag{3}$$

where $t(z)$ is the comoving time at redshift z, $Z_{\rm min}$ and $Z_{\rm max}$ are the minimum and maximum metallicity, $\psi(z')$ is the cosmic star formation rate density at redshift z', $\mathcal{F}(z', z, Z)$ is the fraction of compact binaries that form at redshift z' from stars with metallicity Z and merge at redshift z, and $\eta(Z)$ is the merger efficiency, namely the ratio between the total number of compact binaries (formed from a coeval population) that merge within an Hubble time and the total initial mass of the stellar population with metallicity Z. The cosmological parameters used in equation (3) are taken from Ade et al. (2016). The maximum formation redshift of progenitor binary stars is $z_{\rm max} = 15$. For the cosmic star formation rate $\psi(z')$ we use the fitting formula from Madau & Fragos (2017), while for the evolution of metallicity we use equation (8) of Santoliquido et al. (2021), based on De Cia et al. (2018). Metallicity evolution is extremely uncertain but only has a mild effect on BNS mergers (Dominik et al. 2013; Santoliquido et al. 2021). Hence, this choice almost does not affect our results. We obtain a local merger rate density $\mathcal{R}(z = 0) = 31$,

[1]The horizon is the farthest distance at which a source with optimal sky location and binary inclination can be detected above a threshold signal-to-noise ratio (SNR), generally defined as SNR = 8.

258, and 765 $\mathrm{Gpc^{-3}\ yr^{-1}}$, for the simulation set with $\alpha = 1$, 3, and 7, respectively (Table 1). These values approximately bracket the 90 per cent credible interval estimated by the LIGO–Virgo–KAGRA Collaboration in the GWTC-2.1 catalogue (The LIGO Scientific Collaboration et al. 2021a): $\mathcal{R} = 286^{+510}_{-237}\ \mathrm{Gpc^{-3}\ yr^{-1}}$. This rate was inferred by the LIGO–Virgo-KAGRA Collaboration assuming a BNS population uniform in component masses between 1.0 and 2.5 $\mathrm{M_\odot}$. The GWTC-3 population paper (The LIGO Scientific Collaboration et al. 2021b) recently reported a larger interval $\mathcal{R} =$ 13–1900 $\mathrm{Gpc^{-3}\ yr^{-1}}$, which comes from the union of the 90 per cent credible intervals of several population models, based on different assumptions for the BNS mass function.

Here, we only show models with rate $\mathcal{R}(z = 0) \in [31, 765]\ \mathrm{Gpc^{-3}\ yr^{-1}}$, because rates outside this range are extremely difficult to produce with astrophysically motivated models. Namely, rates lower than $\sim$30 $\mathrm{Gpc^{-3}\ yr^{-1}}$ can be achieved only with extremely large natal kicks (e.g. Santoliquido et al. 2021). Rates higher than $\sim$800 $\mathrm{Gpc^{-3}\ yr^{-1}}$ are almost impossible to obtain with astrophysical models (O'Shaughnessy, Kalogera & Belczynski 2010; de Mink & Belczynski 2015; Kruckow et al. 2018; Mapelli & Giacobbo 2018; Vigna-Gómez et al. 2018; Artale et al. 2019; Eldridge, Stanway & Tang 2019; Neijssel et al. 2019; Giacobbo & Mapelli 2020; Zevin et al. 2020; Broekgaarden et al. 2021; Mandel & Broekgaarden 2022), unless we allow Hertzsprung gap stars to survive a common envelope phase (Dominik et al. 2013; Chruslinska et al. 2018). Hereafter, we refer to the simulation sets with $\alpha = 1$, 3, and 7 as models A1, A3, and A7.

3 THE GW SIMULATIONS

For each of the catalogues of BNSs described in Section 2, we extracted 10^5 binaries and simulated the associated GW signals. To simulate the GW signal associated with each merger we need the mass, sky position, and spin of each system. We used the masses of the two NSs as reported in the catalogues. We assumed an isotropic and homogeneous distribution in space for our BNSs; we also assigned a random inclination of the orbital plane with respect to the line-of-sight θ_j to each BNS. As in Patricelli et al. (2016), for simplicity we considered non-spinning systems, as the NS spin is expected to be small in compact binaries. In fact, only low-spin BNS have been observed through EM waves up to date: the most rapidly rotating pulsar found in a binary system, i.e. PSR J0737−3039A, has a period of $\sim$22.7 ms (Burgay et al. 2003; Brown et al. 2012), corresponding to a very low spin:[2] $\chi \sim 0.05$. However, it is worth to mention that the fastest spinning observed millisecond pulsar, i.e. PSR J1748−2446ad, has a lower period of $\sim$1 ms (Hessels et al. 2006) and then a higher spin: $\chi \sim 0.4$; furthermore, even higher values are allowed by theoretical models.

For each merging BNS, we simulated the expected GW inspiral signals using the 'TaylorT4' waveforms (see e.g. Buonanno et al. 2009) that are constructed using post-Newtonian models accurate to the 3.5 order in phase and 1.5 order in amplitude. Then, we added the GW signal to the detector noise, assumed to be Gaussian. We considered a GW network composed of Advanced LIGO, Advanced Virgo, and KAGRA, and used the sensitivity curves expected for O4 (Abbott et al. 2020a). Specifically, we used the public sensitivities:[3] an intermediate-sensitivity curve for KAGRA, corresponding to a BNS range of 80 Mpc, and the target sensitivity curve (the highest O4 sensitivity) for Advanced LIGO and for Advanced Virgo, corresponding to a BNS range of 190 and 120 Mpc, respectively. The data obtained in this way have been then analysed with the matched filtering technique (Wainstein & Zubakov 1962). We consider two different scenarios to estimate the GW detection rates. In the first scenario, hereafter 'case a' we assume a source to be detected if it has a signal-to-noise ratio (SNR) larger than 4 in at least two detectors and a network SNR larger than 12, similarly to what has been done in Patricelli et al. (2016) and Abbott et al. (2020a). We then consider another scenario ('case b') in which a BNS merger is assumed to be detected if it has a network SNR larger than 8, even if observed with a single interferometer, as done in Petrov et al. (2022). This last approach is representative of the public GW alerts sent during the third LIGO–Virgo–KAGRA observing run (O3); however, it is important to mention that a lower SNR threshold could imply a larger contamination by noise events, and that 30 per cent of the O3 alerts have been retracted.[4] In both scenarios we assume that each GW detector has an independent duty cycle of 70 per cent and consider an observing period of 1 yr, i.e. the expected duration of O4 (Abbott et al. 2020a). For the detected sources, we produced the associated three-dimensional GW sky maps with BAYESTAR, a rapid Bayesian position reconstruction code that computes source location using the output from the detection pipelines (Singer et al. 2014, 2016). The matched-filter pipeline and the sky localization have been simulated using the `bayestar-realize-coincs` and `bayestar-localize-coincs` tools from the LIGO.SKYMAP public library.[5]

The GW detection rates have been estimated by combining the BNS merger rate density and the percentage of detected BNS systems.

4 THE ASSOCIATED GRB EMISSION

In order to evaluate the joint GW–EM detection, in what follows we assumed that all BNS mergers give rise to an S-GRB.

4.1 The prompt emission

We associated a set of simulated parameters describing the prompt emission of S-GRBs to each BNS merger: the rest-frame peak energy of the prompt emission spectrum E_pk, the isotropic bolometric peak luminosity L_iso, the redshift z of the BNS merger, and the observer's viewing angle, which corresponds to the inclination of the BNS system θ_j.

Following the methodology presented in Ghirlanda et al. (2016, hereafter G16), we assigned to each BNS merger a value of E_pk drawn randomly from a broken power-law distribution (see G16, equation 13, with the parameters reported in Table 1, case a) and a value of L_iso sampled from a lognormal distribution whose central value is given by the E_pk–L_iso correlation (Yonetoku et al. 2004, written as in G16, equation 14) and $\sigma = 0.2$ to account for the uncertainty in the parameters of the correlation. The average values for the E_pk and L_iso obtained with this procedure are $\langle E_\mathrm{pk}\rangle = 700$ keV and $\langle L_\mathrm{iso}\rangle = 2 \times 10^{52}\ \mathrm{erg\ s^{-1}}$, and the minimum and maximum values allowed are $E_\mathrm{pk}^\mathrm{min} = 0.1$ keV and $E_\mathrm{pk}^\mathrm{max} = 10^5$ keV, and $L_\mathrm{iso}^\mathrm{min} \sim 4 \times 10^{45}\ \mathrm{erg\ s^{-1}}$ and $L_\mathrm{iso}^\mathrm{max} \sim 4 \times 10^{55}\ \mathrm{erg\ s^{-1}}$.

[2] χ is defined as $c\,J/G\,M^2$, where c is the speed of light, G is the gravitational constant, and J and M are the angular momentum and the mass of the star, respectively.

[3] https://dcc.ligo.org/LIGO-T2000012/public

[4] https://gracedb.ligo.org/superevents/public/O3/

[5] https://lscsoft.docs.ligo.org/ligo.skymap/

Table 1. Expected rates of GW and joint GW+EM detection of BNS mergers and the associated GRB prompt emission for the three BNS models considered in this work for the most conservative scenario for the GW detection (case a); the local BNS merger rate density $\mathcal{R}(0)$ is also reported. The rates for the joint GW+EM detection are computed for a uniform jet with aperture $\theta_c = 5^\circ$ ($\theta_c = 10^\circ$) and for a structured jet. In this case, the range reported corresponds to the minimum and maximum rate obtained for the different structures of the jet assumed.

Model			GW+EM (prompt)							
			Swift/BAT		*Fermi*/GBM		*INTEGRAL*/IBIS		*SVOM*/ECLAIRs	
	$\mathcal{R}(0)$ (Gpc^{-3} yr^{-1})	GW (yr^{-1})	Uniform (yr^{-1})	Structured (yr^{-1})	Uniform (yr^{-1})	Structured (yr^{-1})	Uniform (yr^{-1})	Structured (yr^{-1})	Uniform (yr^{-1})	Structured (yr^{-1})
A1	31	1	0.0006 (0.0023)	0.014–0.020	0.003 (0.013)	0.070–0.11	0.0001 (0.0004)	0.0024–0.0035	0.0005 (0.0019)	0.013–0.017
A3	258	5	0.003 (0.01)	0.07–0.10	0.017 (0.068)	0.35–0.54	0.0005 (0.002)	0.01–0.02	0.002 (0.01)	0.06–0.08
A7	765	13	0.008 (0.031)	0.18–0.26	0.045 (0.18)	0.91–1.42	0.001 (0.005)	0.031–0.046	0.006 (0.025)	0.17–0.22

We assumed as first approximation that the outflow of S-GRBs is a uniform jet, namely that the radiated energy and Lorentz factor are uniformly distributed inside a narrow jet with an opening angle θ_c, and we explored two cases: $\theta_c = 5^\circ$ and 10° (Fong et al. 2015; G16). Then, for S-GRBs associated with *on-axis* BNS mergers (i.e. BNS mergers with inclination $\theta_j < \theta_c$), we calculated the observed photon flux P_{pk} in the energy band $[E_{min}, E_{max}]$ corresponding to a specific instrument as

$$P_{pk} = \frac{(1+z)\int_{(1+z)E_{min}}^{(1+z)E_{max}} S(E)\,dE}{4\pi\, d_L^2}, \quad (4)$$

where d_L is the luminosity distance at redshift z and $S(E)$ is a Band photon spectrum whose normalization is such that

$$L_{iso} = \int_{E_1}^{E_2} S(E) E\,dE, \quad (5)$$

with $[E_1, E_2] = [1, 10]$ keV. For the Band spectrum, we assumed a constant value for the low and high photon spectral indices $\alpha_1 = -0.6$ and $\alpha_2 = -2.5$, respectively, representative of the spectral indices of the population of S-GRBs observed by *Fermi*/GBM and well fitted to a Band function (Gruber et al. 2014). We keep these two parameters fixed after checking that our results are unaffected by sampling them from distributions centred around these values (see also G16).

We also explored a more reliable scenario by modelling the GRB outflow as a structured jet with two possible intrinsic structures for the radiated luminosity per jet unit solid angle and the Lorentz factor of the emitting material Γ_o (Salafia et al. 2015, 2019).

(i) A power-law distribution:

$$\frac{dL}{d\Omega}(\theta) = \frac{L_{iso}/4\pi}{1+(\theta/5^\circ)^s}, \quad \Gamma_o(\theta) = 1 + \frac{\Gamma_o - 1}{1+(\theta/5^\circ)^p}. \quad (6)$$

The power-law index s in the angular distribution of the radiated energy is allowed to vary within the range 3.5–5.5, as estimated for GRB 170817A (see e.g. D'Avanzo et al. 2018 or Ghirlanda et al. 2019). For the Lorentz factor, we assumed that $\Gamma_o = 250$ and $p = 2$ (Ghirlanda et al. 2019).

(ii) A Gaussian distribution:

$$\frac{dL}{d\Omega}(\theta) = \frac{L_{iso}}{4\pi} e^{-(\theta/5^\circ)^2}, \quad \Gamma_o(\theta) = 1 + (\Gamma_o - 1) e^{-(\theta/5^\circ)^2}, \quad (7)$$

with $\Gamma_o = 250$ (Ghirlanda et al. 2019).

The isotropic-equivalent luminosity observed at a viewing angle θ_j is then computed as (Salafia et al. 2015, 2019)

$$L_{iso}(\theta_j) = \int \frac{\delta^3(\theta, \phi, \theta_j)}{\Gamma_o(\theta)} \frac{dL}{d\Omega}(\theta)\, d\Omega, \quad (8)$$

where δ is the relativistic Doppler factor.

This allowed us to considered also the contribution to the detection rate by S-GRBs associated with moderately off-axis BNS mergers by calculating from equation (8) the isotropic-equivalent radiated luminosity for an observer at a viewing angle θ_j with $5^\circ < \theta_j < 35^\circ$. Assuming that the E_{pk}–L_{iso} correlation also holds for moderately off-axis S-GRBs, we calculated $E_{pk}(\theta_j)$ from $L_{iso}(\theta_j)$. While this assumption has been proved in simulations of the prompt emission of off-axis GRBs (see e.g. Salafia et al. 2015, 2019), notably this is not the case for GRB 170817A. More detailed modelling of the prompt emission from off-axis S-GRBs is beyond the scope of this work.

4.2 The X-ray afterglow emission

Despite the number of high-energy satellites in operation with instrumentation dedicated to the detection of GRBs, it is possible that an S-GRB on-axis or moderately off-axis is not detected during its prompt phase. This happens because even all-sky detectors (like *Fermi*/GBM) have relatively limited duty cycles due to observational constraints (see Appendix A). However, it is still possible to discover them by searching for their afterglows with dedicated facilities that are capable of tiling large regions in the sky and discover new transient sources in those regions. While for the X-ray afterglow emission we can rely on the robust and homogeneous sample collected with *Swift*/X-Ray Telescope (XRT),[6] the sample of S-GRB afterglow light curves observed in the optical and radio bands is much more sparse, with less than ∼40 per cent and ∼10 per cent of the *Swift* S-GRBs having an optical and radio afterglow, respectively, detected (Fong et al. 2015). The optical and radio samples are therefore severely affected by selection effects. We thus evaluated how many BNS mergers leading to S-GRBs meet the optimal conditions for being discovered by facilities operating in the X-ray band. In what follows, we assume the strategy put in place by *Swift*/XRT during the O3 run as a reference (Evans et al. 2016a,b; for details see Appendix A).

The first requirement is that the sky map is a single region with a 90 per cent confidence area ≤50 deg^2. This choice maximizes the coverage of the whole region with a reasonable exposure time within ∼1 d (Evans et al. 2016b), i.e. when the source is brighter. Then, in order to evaluate the detectability of the S-GRB X-ray emission at different times after the GW trigger, we took the sample presented in D'Avanzo et al. (2014) as reference for the population of on-axis S-GRBs, i.e. S-GRBs associated with BNS mergers with inclination θ_j

[6] ∼90 per cent of the S-GRBs detected by *Swift* for which the satellite carried out a prompt slew has an afterglow detected by *Swift*/XRT.

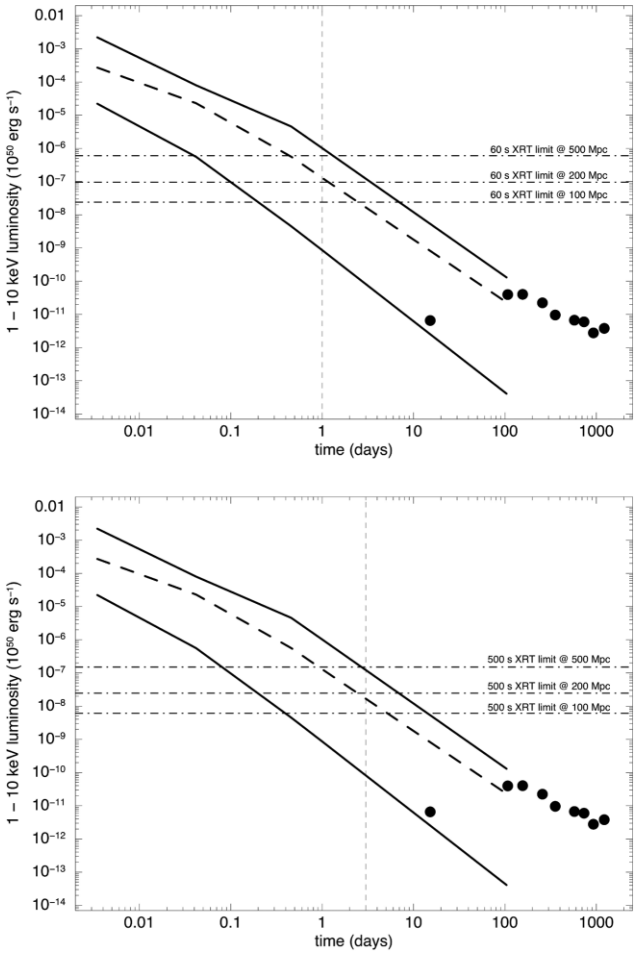

Figure 1. The distribution of S-GRB light curves of the S-BAT4 sample (D'Avanzo et al. 2014). The X-ray luminosities were computed for each GRB in the common rest-frame 1–10 keV energy band following the procedure described in Section 4.2. The dashed line shows the median behaviour; the two solid lines represent the 25 and 75 percentiles. The X-ray afterglow of GW 170817/GRB 170817 is shown with black points for reference (adapted from Hajela et al. 2022). The dashed–dotted lines represent the depths that can be reached with *Swift*/XRT with the current strategy for GW follow-up.

$< \theta_c$ with $\theta_c = 5^\circ$ (see Section 4.1). For each event of the sample we estimated the afterglow X-ray isotropic-equivalent luminosity in the 1–10 keV rest-frame common energy band $L_{X,rf}^{1-10}$ from the observed integral 0.3–10 keV unabsorbed flux $f_X^{0.3-10}$ in the following way (see D'Avanzo et al. 2014):

$$L_{X,rf}^{1-10} = 4\pi d_L^2 f_X^{0.3-10} \frac{\left(\frac{10}{1+z}\right)^{2-\Gamma} - \left(\frac{1}{1+z}\right)^{2-\Gamma}}{10^{2-\Gamma} - 0.3^{2-\Gamma}}, \quad (9)$$

where Γ is the measured spectral index that we retrieved from the online *Swift* Burst Analyser[7] (Evans et al. 2009, 2010). The resulting X-ray afterglow light curves have been compared with the limiting luminosity that can be reached by *Swift*/XRT at different distances within the volume sampled in this work to calculate the fraction of on-axis BNS mergers that can be discovered within the first day or, in case of a non-detection during the first day, the fraction of mergers that are detectable in the following days with longer exposures (Fig. 1; see Appendix A).

[7]https://www.swift.ac.uk/burst_analyser

Under the assumption of a structured jet outflow (see Section 4.1), we can also extend the possible detection to off-axis S-GRBs ($\theta_j > 5^\circ$), by requiring that their X-ray emission peaks during the first ∼10 d after the merger in order to be effectively discovered during the monitoring of the error region. An estimate of the peak time as a function of the viewing angle can be obtained from $t_{pk} \sim 2.1\, E_{k,52}^{1/3} n^{-1/3} ((\theta_j - 5^\circ)/10^\circ)^{8/3}$ d (see Margutti et al. 2018, from Granot & Sari 2002; Granot et al. 2002), where $E_{k,52}$ is the GRB kinetic energy E_k, in units of 10^{52} erg, that can be obtained from E_{iso} via an efficiency factor: $E_k = E_{iso}/\eta$, and n is the particle number density of the circumstellar medium. By assuming that $\langle E_{iso} \rangle = \langle L_{iso} \rangle /2 \sim 10^{52}$ erg, $\eta = 0.1$, and $n = 10^{-3}$ cm^{-3}, we expect that the afterglow peaks at ∼6 d for $\theta_j \sim 10^\circ$. This simple estimate shows that the discovery of the X-ray counterpart of BNS mergers with $\theta_j > 10^\circ$ with facilities as *Swift*/XRT is highly unlikely. As a reference, in Fig. 1 we portray the X-ray light curve of GRB 170817A that has an inclination of $\theta_j \sim 20^\circ$.

5 RESULTS

Tables 1 and 2 show the expected number of GW detections in the 1-yr O4 science run for the first and the second scenario, respectively. When the first scenario is considered, the number of detections ranges from 1 to 13 events per year, depending on the theoretical model used to simulate the population of BNS mergers. These numbers are within the range predicted in Abbott et al. (2020a), where a much larger range of values for the local BNS merger rate density has been considered. When a lower SNR threshold is considered and observations with a single interferometer are included, the number of detections ranges instead from 5 to 61 events per year: there is therefore an increase by a factor of ∼5. These numbers are consistent with the rate of BNS detections predicted for O4 by Petrov et al. (2022), taking into account the difference in the assumed range of values for the BNS merger rate density.

Then, we evaluated the fraction of mergers that give rise to an S-GRB whose prompt emission is detectable by the main GRB facilities. A description of these facilities and the assumptions adopted for the energy band, detection threshold, field of view (FOV), and duty cycle are reported in Appendix A. Tables 1 and 2 show our results for the two GW detection scenarios (case a and case b), respectively. In the uniform jet scenario, the EM–GW joint detection rate is highly suppressed by the geometry of the jet. In fact the fraction of GW events with inclination lower than 5° (10°) is 0.6 per cent (2.5 per cent).

Similar results were found in G16 with the same population. In G16, the detection rate of S-GRBs within a radius of 450 Mpc is ∼0.08 yr^{-1}, without any a priori assumption on the jet opening angle and BNS merger rate. Since they do not make specific assumptions on the detection instrument, we compared this figure with the rate obtained for *Fermi*/GBM corrected for its limited duty cycle. With all these caveats, we find a fair agreement with our rates for the uniform jet case, with closer values for the model A3. Since the rate in G16 has been derived using all the available observer-frame constraints of the large population of *Fermi* S-GRBs and the rest-frame properties of a complete sample of S-GRBs detected by *Swift*, the consistency we find with the predictions derived by G16 ensures that our detection rates are consistent with the observed rates for *Swift* and *Fermi*.

Indeed, GRB 170817A showed that the outflow of S-GRBs is likely structured, allowing for a possible detection of their prompt emission even when they are observed at larger viewing angles. Since our knowledge of the jet structure is limited to one case, we considered different possibilities for the jet structure to cover a

Table 2. Same as Table 1, but assuming a lower network SNR threshold of 8 for the GW detections and including the GW signals detected with a single interferometer (case b).

Model			GW+EM (prompt)							
			Swift/BAT		*Fermi*/GBM		*INTEGRAL*/IBIS		*SVOM*/ECLAIRs	
	$\mathcal{R}(0)$ ($\mathrm{Gpc^{-3}\ yr^{-1}}$)	GW ($\mathrm{yr^{-1}}$)	Uniform ($\mathrm{yr^{-1}}$)	Structured ($\mathrm{yr^{-1}}$)	Uniform ($\mathrm{yr^{-1}}$)	Structured ($\mathrm{yr^{-1}}$)	Uniform ($\mathrm{yr^{-1}}$)	Structured ($\mathrm{yr^{-1}}$)	Uniform ($\mathrm{yr^{-1}}$)	Structured ($\mathrm{yr^{-1}}$)
A1	31	5	0.002 (0.01)	0.05–0.08	0.014 (0.06)	0.27–0.46	0.0005 (0.002)	0.009–0.014	0.002 (0.008)	0.05–0.07
A3	258	22	0.01 (0.04)	0.24–0.37	0.06 (0.26)	1.17–2.00	0.002 (0.008)	0.04–0.06	0.009 (0.04)	0.22–0.32
A7	765	61	0.03 (0.12)	0.67–1.05	0.18 (0.74)	3.28–5.65	0.006 (0.02)	0.11–0.18	0.02 (0.10)	0.63–0.90

Table 3. Expected rates of joint GW+EM detection of BNS mergers and the associated GRB prompt emission for the three BNS models and the two scenarios for the GW detection considered in this work (case a and case b); these rates are computed assuming an intrinsic structure of the jet with a Gaussian distribution.

Model	GW+EM (prompt)							
	Swift/BAT		*Fermi*/GBM		*INTEGRAL*/IBIS		*SVOM*/ECLAIRs	
	Case a ($\mathrm{yr^{-1}}$)	Case b ($\mathrm{yr^{-1}}$)	Case a ($\mathrm{yr^{-1}}$)	Case b ($\mathrm{yr^{-1}}$)	Case a ($\mathrm{yr^{-1}}$)	Case b ($\mathrm{yr^{-1}}$)	Case a ($\mathrm{yr^{-1}}$)	Case b ($\mathrm{yr^{-1}}$)
A1	0.015	0.06	0.073	0.28	0.0025	0.01	0.013	0.05
A3	0.017	0.25	0.37	1.24	0.010	0.04	0.07	0.24
A7	0.19	0.71	0.96	3.44	0.032	0.12	0.17	0.66

broad range of possibilities. The minimum and maximum detection rates correspond both to the power-law intrinsic structure with the steeper and shallower indices, respectively. The Gaussian intrinsic structure gives detection rates within these ranges (see Table 3). The structured S-GRB outflow increases the detection rate by a factor of ∼20–40 with respect to the case of a uniform jet with an aperture $\theta_c = 5^\circ$ (a factor of ∼5–8 for $\theta_c = 10^\circ$). For the structured jet case, the fraction of GW events with joint EM detection is ∼1–2 per cent for *Swift*/Burst Alert Telescope (BAT), 7–11 per cent for *Fermi*/GBM, and 0.2–0.3 per cent for *INTEGRAL*//Imager on Board *INTEGRAL* Satellite (IBIS), depending on the jet structure. These figures translate to a joint GW and EM detection rate that is $\sim 1\ \mathrm{yr^{-1}}$ for *Fermi*/GBM in the most favourable case (model A7) when we consider the most conservative scenario (case a, see Table 1). Although obtained under different assumptions, the expected rate of joint GW and GRB detection with *Fermi*/GBM is consistent with the estimate reported in Abbott et al. (2022). Perspectives for a joint GW–EM detection for the prompt emission are more promising allowing for a lower SNR threshold and less interferometers for the GW detection (case b, see Table 2). In this scenario, we expect several detections per year for *Fermi*/GBM, and up to one detection per year for *Swift*/BAT for model A7.

We also considered the possibility to discover the EM counterpart of the GW-detected events in X-rays with instruments like *Swift*/XRT. Fig. 1 portrays the distribution of the X-ray luminosity of on-axis S-GRBs compared with the limiting luminosity for *Swift*/XRT at 100, 200, and 500 Mpc (see Appendix A). About 60 per cent (50 per cent) of S-GRBs at 100 Mpc (200 Mpc) would be detectable by *Swift*/XRT 1 d after the merger with an exposure of 60 s, while ∼55 per cent (45 per cent) would be still detectable after 3 d in case of a revisit with an exposure of 500 s. This percentage decreases if we move our horizon to 500 Mpc (∼30 per cent at 1 d and 60 s exposure; ∼25 per cent at 3 d and 500 s exposure). We thus evaluated the number of GW-detected BNS mergers within these horizons (100, 200, and 500 Mpc) with optimal characteristics for being discovered by *Swift*/XRT within the first few days, namely being on-axis ($\theta_j < 5^\circ$) and with a good localization (90 per cent confidence region $<50\ \mathrm{deg^2}$). In the most conservative scenario (case a), this is ∼0.5 per cent of the GW-detected BNS mergers in the same volume. In the less conservative scenario (case b) the expected rate increases, but less than for the GW detection rate since the detection with lower SNR and less detector provides a less accurate localization. Convolving these rates with the probability that the X-ray luminosity is above the flux limit at that distance, as described above, we can estimate the rate of X-ray counterparts associated with S-GRBs of GW-detected BNS mergers observable by *Swift*/XRT within different volumes during the first day or the following days of observation (see Table 4). If we consider mergers with $\theta_j < 10^\circ$, namely on-axis S-GRBs with a wider core or moderately off-axis S-GRBs that peak within a few days after the merger, rates rise up to about a factor of 4. In all cases, the rate of S-GRB associated with detectable GW events remains very low, due to the limited volume sampled by these searches and by the requirement to observe the S-GRB nearly on-axis.

6 DISCUSSION AND CONCLUSIONS

We presented a comprehensive study on the expectations for joint GW and EM detection of BNS mergers in the next observing run of Advanced LIGO, Advanced Virgo, and KAGRA (O4), considering different EM facilities: *Fermi*, *Swift*, *INTEGRAL*, and *SVOM*.

Depending on the population synthesis model considered, we expect to have from 1 to 13 BNS merger detections per year when a conservative approach is considered (case a). The number of detections per year increases by a factor of ∼5 when we include the possibility to detect BNS mergers with a single interferometer and with a reduced network SNR threshold (case b, as done in Petrov et al. 2022). It is also worth to mention that the sensitivity of KAGRA during O4 could be lower than the one considered in this work (see https://www.ligo.org/scientists/GWEMalerts.php). However, this is not expected to affect our results in a significant way, since the main contribution to the GW detection rate comes from the more sensitive Advanced LIGO and Advanced Virgo detectors. For instance, if we assume that the KAGRA sensitivity is of the order of 1 Mpc for the whole duration of O4, the decrease in the GW detection rate is less than 10 per cent.

Table 4. Expected rates of X-ray counterparts of GW-detected BNS mergers discoverable by *Swift*/XRT within different volumes (<100 Mpc, between 100 and 200 Mpc, and between 200 and 500 Mpc) during the first day of observation with 60 s exposure (upper panel), and between the first and the third day with 500 s exposure (lower panel), for the three BNS models considered in this work and for the two possible scenarios for the GW detection (case a and case b, respectively). The values reported are obtained considering GW-detected BNS mergers with $\theta_j < 5^\circ$ and 90 per cent confidence region <50 deg^2 convolved with the probability that the X-ray luminosity is above the flux limit at the corresponding distance (60 per cent, 50 per cent, and 30 per cent with 60 s exposure, and 55 per cent, 45 per cent, and 25 per cent with 500 s exposure, respectively; see Section 4.2). If we consider mergers with $\theta_j < 10^\circ$, these rates rise up to about a factor of 4.

Model	GW+EM (X-ray afterglow), case a			GW+EM (X-ray afterglow), case b		
	<100 Mpc (yr^{-1})	100–200 Mpc (yr^{-1})	200–500 Mpc (yr^{-1})	<100 Mpc (yr^{-1})	100–200 Mpc (yr^{-1})	200–500 Mpc (yr^{-1})
A1	0.0015–0.0026	0.0007–0.0014	0.0002–0.0006	0.005–0.008	0.002–0.004	0.0007–0.0024
A3	0.007–0.012	0.003–0.007	0.001–0.003	0.019–0.032	0.010–0.019	0.004–0.013
A7	0.021–0.035	0.009–0.017	0.002–0.006	0.098–0.059	0.025–0.050	0.008–0.028
A1	0.0014–0.0017	0.0006–0.0009	0.0002–0.0003	0.004–0.005	0.0018–0.0025	0.0006–0.0012
A3	0.007–0.010	0.003–0.004	0.0008–0.002	0.018–0.021	0.009–0.011	0.003–0.006
A7	0.019–0.023	0.008–0.010	0.001–0.003	0.054–0.064	0.022–0.030	0.007–0.014

Concerning the joint detection of the GW signal and the S-GRB prompt emission, we show that during O4 this is not only possible, but also likely, depending on the jet structure and on the BNS rate. The best perspectives come from *Fermi*/GBM that will likely detect one event, and possibly several events, during O4. The other instruments are limited by their FOV. However, *Swift*/BAT will be capable of detecting up to one event per year, with the major advantage of providing accurate localization and a rapid follow-up in X-rays (see Section 4.2).

The perspectives for the joint GW–EM detections are even more encouraging than what derived in this work based on the *standard* detection of S-GRBs, since there are strategies specifically tailored to increase the sensitivity of the instruments to the counterparts of GW events, as targeted searches for subthreshold events (Goldstein et al. 2019). *Swift*/BAT has implemented the Gamma-ray Urgent Archiver for Novel Opportunities (GUANO;[8] see Tohuvavohu et al. 2020), a pipeline designed for targeted recovery of BAT event-by-event data around the times of compelling astrophysical events to enable sensitive targeted searches as Non-Imaging Transient Reconstruction And TEmporal Search (NITRATES; DeLaunay & Tohuvavohu 2021) that boosts the discovery rate of GRB 170817A-like events in BAT by a factor of at least 3–4. In addition, there are other instruments that can support those considered in this work for a more efficient discovery of S-GRBs. *INTEGRAL*/IBIS is limited by its FOV, but S-GRBs could be also detected by the Anti-Coincidence Shield (ACS) of the Spectrometer onboard *INTEGRAL* (SPI).[9] The SPI-ACS works as a nearly omnidirectional GRB detector above ∼80 keV, but it lacks spatial and spectral information.

SVOM will be a further asset for the discovery of S-GRBs when it will join the O4 run (its launch is expected for mid-2023). *SVOM*/ECLAIRs have similar performances than *Swift*/BAT for the detection of S-GRBs (see Tables 1 and 2) and, since they are not likely monitoring the same region of the sky, together they will almost double the possibility to have a GW event detected during the prompt emission when *SVOM* will be operational. Besides, *SVOM* will also be equipped with a Gamma-Ray Monitor (GRM) with a larger FOV and a higher high-energy threshold (5 MeV) than ECLAIRs that will improve the detection of S-GRBs, although with poor localization (see e.g. Wei et al. 2016; Bernardini et al. 2017).

In the last years other authors investigated the prospects for joint detections of GWs and S-GRBs with different approaches and under different assumptions that led to different estimates of the detection rates. For instance, Song et al. (2019) predicted a joint GW/S-GRB detection rate of 1.83, 0.388, and 0.668 yr^{-1} for *Fermi*/GBM, *Swift*/BAT, and *SVOM*/ECLAIRS, respectively; these estimates are based on the assumption of a local BNS merger rate density of 1540^{+3200}_{-1220} Gpc^{-3} yr^{-1}, a network SNR GW threshold of 16 and of a universal jet profile (the one inferred for GRB 170817A) for all the S-GRBs associated with the BNS Mergers. Assuming the same local BNS merger rate density but a lower SNR GW threshold of 8, Howell et al. (2019) predicted instead a joint GW/S-GRB detection rate of $1.23^{+2.55}_{-0.97}$ yr^{-1} for *Fermi*/GBM. This work differentiates from previous studies for several key aspects. We investigated the joint S-GRB and GW observations by combining accurate population synthesis modelling with pipelines specifically developed to provide GW detections and low-latency GW sky localization: we use theoretically motivated BNS merger rate densities, each one corresponding to a specific physical model and we mimic the real GW data analysis. Furthermore, in the GRB modelling we do not rely on the properties of GRB 170817A only, but we simulated the whole S-GRB population starting from reliable assumptions (the luminosity function derived in G16 using all the available observer-frame constraints of the large population of *Fermi* S-GRBs and the rest-frame properties of a complete sample of S-GRBs detected by *Swift*, and the E_{pk}–L_{iso} correlation) and we explored different possibilities for the jet structure, computing the apparent structure as introduced in Salafia et al. (2015).

The perspectives to observe X-ray counterparts to GW events are not very promising, mainly because we can detect only events pointing towards us ($\theta_j < 10^\circ$). However, the improved localization expected in O4 for nearby events [we will have 52 per cent (45 per cent) of events within 200 Mpc with a 90 per cent credible region (c.r.) <10 deg^2, and 42 per cent (37 per cent) with a 90 per cent c.r. <5 deg^2 for case a (case b)] will permit a faster coverage of the region, catching the candidate when it is brighter.

In this work, we did not explore the contribution to the detection rate of galaxy-targeted searches of EM counterparts. While this approach has revealed itself successful in the case of GW170817, for more distant events this could not be the optimal observational strategy: in fact, current galaxy catalogues are complete only up to a distance of a few tens of Mpc, losing more than half of the brightest galaxies beyond ∼250 Mpc (see e.g. Evans et al. 2016b; Dálya et al. 2021).

Besides S-GRBs, a key signature of a BNS (and possibly NS–black hole) binary merger is the production of a kilonova whose emission

[8] https://www.swift.psu.edu/guano/
[9] https://www.cosmos.esa.int/web/integral/instruments-spi

is characterized by two main components, namely the blue and red kilonova (Metzger 2019). The red kilonova component emission is expected to be nearly isotropic and to peak in the optical/near-infrared bands, while the blue kilonova (whose emission peaks in the ultraviolet/optical band) might not be present in all BNS mergers (Metzger et al. 2015) and, even if present, its emission is expected to be angle dependent (i.e. the brightness can depend on the line of sight; Kasen et al. 2017). Recently, Andreoni et al. (2021) highlighted that realistic predictions on joint GW–kilonova detection should conservatively built around the capability to detect the red kilonova component. In their work, the authors show that a firm detection of red kilonovae during O4 can be obtained only within ∼100 Mpc, while for joint GW–kilonova detection beyond such horizon we will have to wait for O5, when the Vera C. Rubin Observatory will be operational. From our study, we estimate that during O4 the rate of GW-detected BNS mergers within 100 Mpc is 0.6–8 yr^{-1} for case a and 2–23 yr^{-1} for case b, depending on the model considered, and all these events are possible targets for the search of the associated red kilonova.

All the results presented in this paper take into account the current theoretical uncertainties on the BNS merger rate density, as well as our poor knowledge of the GRB population and of the jet structure. A direct comparison of these results with future joint GW–EM observations will narrow down most of these unknowns, shedding light on the physics of compact objects and on the association between S-GRBs and BNS system, as well as on the GRB jet geometry. Indeed, there is a realistic probability to observe at least another multimessenger event during O4, provided that EM facilities such as *Fermi*/GBM and *Swift*/BAT will be operating. As demonstrated by the case of GW170817/GRB 170817A, such an achievement would lead to a significant scientific advancement in the newly born field of multimessenger astronomy. As highlighted in this work, this will be possible only with dedicated time-domain programs of space and ground-based facilities with the necessary suite of capabilities required to detect and follow-up EM counterparts to GW events (see e.g. 'Pathways to Discovery in Astronomy and Astrophysics for the 2020s', the National Academies of Science, Engineering and Medicine's latest decadal survey).[10]

ACKNOWLEDGEMENTS

We are grateful to the referee for the very valuable comments and suggestions. We thank Sergio Campana for useful discussions. MM and FS acknowledge financial support from the European Research Council for the ERC Consolidator grant DEMOBLACK, under contract no. 770017. BP acknowledges financial support from the ESCAPE project with grant no. GA:824064. This work makes use of the LIGO.SKYMAP scientific software package (https://lscsoft.docs.ligo.org/ligo.skymap/).

DATA AVAILABILITY

The data underlying this paper will be shared on reasonable request to the corresponding author.

REFERENCES

Aasi J. et al., 2015, Classical Quantum Gravity, 32, 074001
Abbott B. P. et al., 2017a, Phys. Rev. Lett., 119, 161101
Abbott B. P. et al., 2017b, ApJ, 848, L13
Abbott B. P. et al., 2020a, Living Rev. Relativ., 23, 3
Abbott B. P. et al., 2020b, ApJ, 892, L3
Abbott R. et al., 2021, ApJ, 913, L7
Abbott R. et al., 2022, ApJ, 928, 186
Acernese F. et al., 2015, Classical Quantum Gravity, 32, 024001
Ade P. A. R. et al., 2016, A&A, 594, A13
Akutsu T. et al., 2019, Classical Quantum Gravity, 36, 165008
Andreoni I. et al., 2021, preprint (arXiv:2111.01945)
Artale M. C., Mapelli M., Giacobbo N., Sabha N. B., Spera M., Santoliquido F., Bressan A., 2019, MNRAS, 487, 1675
Bernardini M. G. et al., 2017, Exp. Astron., 44, 113
Broekgaarden F. S. et al., 2021, MNRAS, 508, 5028
Brown D. A., Harry I., Lundgren A., Nitz A. H., 2012, Phys. Rev. D, 86, 084017
Buonanno A., Iyer B. R., Ochsner E., Pan Y., Sathyaprakash B. S., 2009, Phys. Rev. D, 80, 084043
Burgay M. et al., 2003, Nature, 426, 531
Chruslinska M., Belczynski K., Klencki J., Benacquista M., 2018, MNRAS, 474, 2937
Coulter D. A. et al., 2017, Science, 358, 1556
Dagoneau N., Schanne S., Rodriguez J., Atteia J. L., Cordier B., 2021, A&A, 645, A18
Dálya G. et al., 2021, preprint (arXiv:2110.06184)
D'Avanzo P. et al., 2014, MNRAS, 442, 2342
D'Avanzo P. et al., 2018, A&A, 613, L1
De Cia A., Ledoux C., Petitjean P., Savaglio S., 2018, A&A, 611, A76
DeLaunay J., Tohuvavohu A., 2021, preprint (arXiv:2111.01769)
de Mink S. E., Belczynski K., 2015, ApJ, 814, 58
Dominik M., Belczynski K., Fryer C., Holz D. E., Berti E., Bulik T., Mandel I., O'Shaughnessy R., 2013, ApJ, 779, 72
Eldridge J. J., Stanway E. R., Tang P. N., 2019, MNRAS, 482, 870
Evans P. A. et al., 2009, MNRAS, 397, 1177
Evans P. A. et al., 2010, A&A, 519, A102
Evans P. A. et al., 2016a, MNRAS, 455, 1522
Evans P. A. et al., 2016b, MNRAS, 462, 1591
Fong W., Berger E., Margutti R., Zauderer B. A., 2015, ApJ, 815, 102
Fryer C. L., Belczynski K., Wiktorowicz G., Dominik M., Kalogera V., Holz D. E., 2012, ApJ, 749, 91
Gehrels N. et al., 2004, ApJ, 611, 1005
Ghirlanda G. et al., 2016, A&A, 594, A84(G16)
Ghirlanda G. et al., 2019, Science, 363, 968
Giacobbo N., Mapelli M., 2018, MNRAS, 480, 2011
Giacobbo N., Mapelli M., 2019, MNRAS, 482, 2234
Giacobbo N., Mapelli M., 2020, ApJ, 891, 141
Giacobbo N., Mapelli M., Spera M., 2018, MNRAS, 474, 2959
Goldstein A. et al., 2017, ApJ, 848, L14
Goldstein A. et al., 2019, preprint (arXiv:1903.12597)
Granot J., Sari R., 2002, ApJ, 568, 820
Granot J., Panaitescu A., Kumar P., Woosley S. E., 2002, ApJ, 570, L61
Gruber D. et al., 2014, ApJS, 211, 12
Hajela A. et al., 2022, ApJ, 927, L17
Hallinan G. et al., 2017, Science, 358, 1579
Hessels J. W. T., Ransom S. M., Stairs I. H., Freire P. C. C., Kaspi V. M., Camilo F., 2006, Science, 311, 1901
Hobbs G., Lorimer D. R., Lyne A. G., Kramer M., 2005, MNRAS, 360, 974
Hosseinzadeh G. et al., 2019, ApJ, 880, L4
Howell E. J., Ackley K., Rowlinson A., Coward D., 2019, MNRAS, 485, 1435
Hurley J. R., Tout C. A., Pols O. R., 2002, MNRAS, 329, 897
Kasen D., Metzger B., Barnes J., Quataert E., Ramirez-Ruiz E., 2017, Nature, 551, 80
Kroupa P., 2001, MNRAS, 322, 231
Kruckow M. U., Tauris T. M., Langer N., Kramer M., Izzard R. G., 2018, MNRAS, 481, 1908
Kuulkers E. et al., 2021, New Astron. Rev., 93, 101629
Madau P., Fragos T., 2017, ApJ, 840, 39
Mandel I., Broekgaarden F. S., 2022, Living Rev. Relativ., 25, 1

[10] https://nap.edu/resource/26141/interactive/

Mapelli M., Giacobbo N., 2018, MNRAS, 479, 4391
Mapelli M., Giacobbo N., Ripamonti E., Spera M., 2017, MNRAS, 472, 2422
Mapelli M., Spera M., Montanari E., Limongi M., Chieffi A., Giacobbo N., Bressan A., Bouffanais Y., 2020, ApJ, 888, 76
Margutti R. et al., 2018, ApJ, 856, L18
Meegan C. et al., 2009, ApJ, 702, 791
Mereghetti S., Götz D., Borkowski J., Walter R., Pedersen H., 2003, A&A, 411, L291
Metzger B. D., 2019, Living Rev. Relativ., 23, 1
Metzger B. D., Bauswein A., Goriely S., Kasen D., 2015, MNRAS, 446, 1115
Mooley K. P. et al., 2018, Nature, 561, 355
Neijssel C. J. et al., 2019, MNRAS, 490, 3740
O'Shaughnessy R., Kalogera V., Belczynski K., 2010, ApJ, 716, 615
Patricelli B., Razzano M., Cella G., Fidecaro F., Pian E., Branchesi M., Stamerra A., 2016, J. Cosmol. Astropart. Phys., 11, 056
Petrov P. et al., 2022, ApJ, 924, 54
Pian E. et al., 2017, Nature, 551, 67
Ritz S., 2007, in Ritz S., Michelson P., Meegan C. A., eds, AIP Conf. Proc. Vol. 921, The First GLAST Symposium. Am. Inst. Phys., New York, p. 3
Salafia O. S., Ghisellini G., Pescalli A., Ghirlanda G., Nappo F., 2015, MNRAS, 450, 3549
Salafia O. S., Ghirlanda G., Ascenzi S., Ghisellini G., 2019, A&A, 628, A18
Sana H. et al., 2012, Science, 337, 444
Santoliquido F., Mapelli M., Bouffanais Y., Giacobbo N., Di Carlo U. N., Rastello S., Artale M. C., Ballone A., 2020, ApJ, 898, 152
Santoliquido F., Mapelli M., Giacobbo N., Bouffanais Y., Artale M. C., 2021, MNRAS, 502, 4877
Savchenko V. et al., 2017, ApJ, 848, L15
Singer L. P. et al., 2014, ApJ, 795, 105
Singer L. P. et al., 2016, ApJ, 829, L15
Smartt S. J. et al., 2017, Nature, 551, 75
Song H.-R., Ai S.-K., Wang M.-H., Xing N., Gao H., Zhang B., 2019, ApJ, 881, L40
Tanvir N. R. et al., 2017, ApJ, 848, L27
Tauris T. M., Langer N., Moriya T. J., Podsiadlowski P., Yoon S.-C., Blinnikov S. I., 2013, ApJ, 778, L23
Tauris T. M., Langer N., Podsiadlowski P., 2015, MNRAS, 451, 2123
Tauris T. M. et al., 2017, ApJ, 846, 170
The LIGO Scientific Collaboration et al., 2021a, preprint (arXiv:2108.01045)
The LIGO Scientific Collaboration et al., 2021b, preprint (arXiv:2111.03634)
Tohuvavohu A., Kennea J. A., DeLaunay J., Palmer D. M., Cenko S. B., Barthelmy S., 2020, ApJ, 900, 35
Troja E. et al., 2017, Nature, 551, 71
Vigna-Gómez A. et al., 2018, MNRAS, 481, 4009
von Kienlin A. et al., 2020, ApJ, 893, 46
Wainstein L. A., Zubakov V. D., 1962, Extraction of Signals from Noice. Prentice-Hall, Englewood Cliffs, NJ
Webbink R. F., 1984, ApJ, 277, 355
Wei J. et al., 2016, preprint (arXiv:1610.06892)
Winkler C. et al., 2003, A&A, 411, L1
Yonetoku D., Murakami T., Nakamura T., Yamazaki R., Inoue A. K., Ioka K., 2004, ApJ, 609, 935
Zevin M., Spera M., Berry C. P. L., Kalogera V., 2020, ApJ, 899, L1

APPENDIX A: INSTRUMENTS

A1 *Swift*/BAT and XRT

Neil Gehrels Swift Observatory (*Swift*; Gehrels et al. 2004) is a US/UK/Italian multiwavelength space observatory dedicated to the study of GRB science. Launched in 2004 November, it is equipped with three instruments: wide-field hard X-ray burst detection telescope (Burst Alert Telescope – BAT; operating in the 15–150 keV band); narrow-field X-ray telescope (X-Ray Telescope – XRT; operating in the 0.3–10 keV band); and ultraviolet–optical telescope (UV Optical Telescope – UVOT; operating in the 170–600 nm spectral range). These three instruments work together to provide imaging, timing, and spectroscopic observations of GRBs and afterglows in the gamma-ray, X-ray, ultraviolet, and optical wavebands. For *Swift*/BAT, in this work we adopted a duty cycle of 90 per cent, a fraction of the sky covered of FOV/4π with FOV = 1.4 sr and a flux limit for the detection $P_{\rm lim} = 0.6$ photons s^{-1} cm^{-2} in the energy band 15–150 keV. To estimate the *Swift*/XRT performances we took as reference the strategy outlined in Evans et al. (2016b). According to such a strategy, each field of the GW sky map is visited at least twice, with a first visit carried out as soon as possible with exposure time of 60 s and a second visit carried out with a longer exposure (500 s). The pointing capabilities of *Swift* enable to cover $\sim$50 deg^2 d^{-1}. For our purposes, we considered a detection when 5 (10) counts are detected with a 60 s (500 s) exposure. Using WebPIMMS[11] we converted these count/rates into fluxes in the common 1–10 keV energy band (see Section 4.2) assuming a typical GRB spectrum (an absorbed power law with photon index 2) and a Galactic $N_{\rm H} = 3^{20}$ cm^{-2} and then in the corresponding limiting 1–10 keV luminosity at 100, 200, and 500 Mpc.

A2 *Fermi*/GBM

The *Fermi Gamma-ray Space Telescope* (*Fermi*) was launched in 2008 June. The payload comprises two science instruments: the Large Area Telescope (LAT) and the Gamma-ray Burst Monitor (GBM). The GBM (Meegan et al. 2009) is a nearly all-sky monitor, capable to trigger GRBs between $\sim$8 keV and $\sim$40 MeV and to study the spectrum and time history of the GRB prompt emission. In this work, we assumed that the whole sky is monitored with a duty cycle of 60 per cent,[12] and a flux limit for the detection $P_{\rm lim} =$ 0.27 photons s^{-1} cm^{-2} in the energy band 50–300 keV. This value corresponds to the peak flux above which lie 95 per cent of the S-GRBs from the *Fermi*/GBM catalogue (von Kienlin et al. 2020).[13]

A3 *INTEGRAL*/IBIS

INTErnational Gamma-Ray Astrophysics Laboratory (*INTEGRAL*) is a satellite of the European Space Agency, launched in 2002. The instrument used for the GRB detection is IBIS, which provides images in the 15 keV–1 MeV range over a large FOV = 30° × 30° using the coded mask technique (Kuulkers et al. 2021). No onboard triggering system is present on *INTEGRAL*. The search for GRBs is done on ground, where the data arrive with an average delay of $\sim$10 s, in nominal conditions. For this purpose, the *INTEGRAL* Burst Alert System (IBAS) has been implemented for the real time detection of GRBs and the rapid distribution of their coordinates (Mereghetti et al. 2003). In this work, we adopted a duty cycle of 85 per cent (Kuulkers et al. 2021), a fraction of the sky covered of FOV/4π with FOV = 30° × 30° and a flux limit for the detection $P_{\rm lim} = 0.15$ counts s^{-1} cm^{-2} in the energy band 50–300 keV.[14]

A4 *SVOM*/ECLAIRs

Space Variable Objects Monitor (*SVOM*; Wei et al. 2016) is a Sino–French mission that is dedicated to GRB science, expected

[11] https://heasarc.gsfc.nasa.gov/cgi-bin/Tools/w3pimms/w3pimms.pl
[12] https://fermi.gsfc.nasa.gov/ssc/observations/types/grbs/
[13] https://fermi.gsfc.nasa.gov/science/instruments/table1-2.html
[14] http://ibas.iasf-milano.inaf.it/

to be launched in mid-2023. The mission includes four space-based and three ground-based instruments for a complete monitoring of the GRB emission, from the prompt to the late phases of the afterglow. The telescope ECLAIRs is a coded mask instrument with a FOV $=$ 2 sr, capable of triggering and locating GRBs with a precision of less than 12 arcmin in the 4–120 keV energy band. In this work, we adopted a duty cycle of 50 per cent, due to the occultation of the Earth (Wei et al. 2016), a fraction of the sky covered of FOV/4π with FOV $=$ 2 sr and a flux limit for the detection $P_{\rm lim}$ $=$ 1.79 photons s^{-1} cm^{-2} in the energy band 4–120 keV (Dagoneau et al. 2021).

This paper has been typeset from a TEX/LATEX file prepared by the author.